CCS Chemistry

RESEARCH ARTICLE

Received: June 10, 2020 | Accepted: July 27, 2020 | Published: Sept. 14, 2020

Pd(II) and Rh(III) Complexes with Isoquinoline Derivatives Induced Mitochondria-Mediated Apoptotic and Autophagic Cell Death in HepG2 Cells

Noor Shad Gul[1†], Taj-Malook Khan[1†], Yan-Cheng Liu[1], Muhammad Iqbal Choudhary[2], Zhen-Feng Chen[1*] & Hong Liang[1*]

[1]*State Key Laboratory for Chemistry and Molecular Engineering of Medicinal Resources, School of Chemistry and Pharmacy, Guangxi Normal University, Guilin 541004,* [2]*International Center for Chemical and Biological Sciences, University of Karachi, Karachi 74270*

**Corresponding authors: chenzf@gxnu.edu.cn; hliang@gxnu.edu.cn;* [†]N. S. Gul and T.-M. Khan contributed equally to this work.

Cite this: *CCS Chem*. **2020**, *2*, 1626–1641

Nonplatinum metal complexes of $[Pd(L^1)Cl_2]$ (C1), $[Rh(L^1)Cl_3(DMSO)]$ (C2), $[Pd(L^2)Cl_2]$ (C3), and $[Rh(L^3)Cl_3(DMSO)]$ (C4) with isoquinoline derivatives have been prepared and characterized. C1–C4 exhibited higher in vitro anticancer activity and lower toxicity than the corresponding ligands and cisplatin against HepG2 cells. The mechanistic studies revealed that C1 arrested the cell cycle at S-phase by regulation of cyclin and cyclin-dependent kinases. C1 was accumulated in mitochondria, which increased the generation of reactive oxygen species (ROS) and endoplasmic reticulum (ER)-stress response through mitochondrial dysfunction. Moreover, C1 stimulated Ca^{2+} release, activated the caspase cascade, and triggered mitochondria-mediated apoptosis. The in vivo studies of C1 demonstrated higher safety than cisplatin and effective tumor growth inhibition. C1 is a potential anticancer drug candidate.

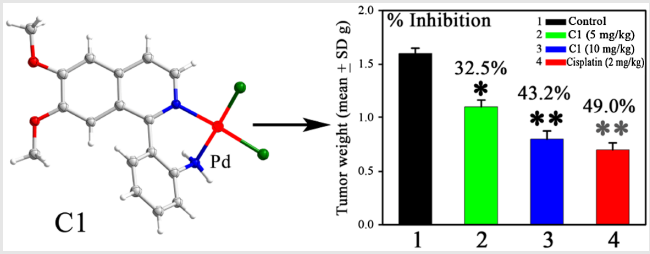

Keywords: **palladium(II), rhodium(III), isoquinoline derivatives, anticancer, apoptosis, autophagy**

Introduction

Platinum drugs, including cisplatin and its analogs carboplatin (Paraplatin) and oxaliplatin (Eloxatin), have been in clinical use to treat various solid tumors.[1–3] Despite clinical success, drug resistance and severe side effects limit their wider use and effectiveness.[4] Therefore, numerous studies have been carried out to develop new drugs with fewer side effects and better chemotherapeutic efficacy than platinum-based drugs.[5] During the past decade, nonplatinum metal complexes such as KP1019, auranofin, NAMI-A, and padeliporfin (TOOKAD) possessing promising anticancer activity against various kinds of cancers with different anticancer mechanisms are reported. Some of these complexes are now in different phases of clinical trials.[6,7] In addition, palladium(II),

DOI: 10.31635/ccschem.020.202000363
Citation: *CCS Chem*. **2020**, 2, 1626–1641
Citation denotes calendar and volume year of first online publication.
Issue Assignment: Volume 3 (2021), Issue 6

rhodium(III), and copper(II) complexes are shown to exhibit higher anticancer activity toward various human cancer cells than platinum-based drugs.[8–10]

In this regard, palladium(II) complexes presented different anticancer properties against breast, lung, and prostate cancers than cisplatin.[11,12] The palladium complexes with ethyl and benzyl amines induced apoptosis and DNA damage by activating the p53 protein and causing cell cycle arrest.[13–17] In addition, several palladium complexes with triazole, pyrazole, and pyrrole as ligands induced reactive oxygen species (ROS)-mediated apoptosis.[18] In ROS-mediated apoptosis, the intrinsic pathway is responsible for the release of cytochrome C and the activation of caspases, which regulate the Bcl-2 family proteins and ultimately lead to cell death.[19,20] Many palladium complexes with imidazole and pyridine ligands produce high levels of ROS and reactive nitrogen species (RNS) that not only increase the risk of mutation and inhibit cell division but also induce apoptosis if the stress persists.[21]

Similarly, rhodium(III) complexes with polyaromatic ligands have potent anticancer activities against various kinds of cancers, such as colon and breast cancers.[22] Mechanistic studies revealed that these complexes target DNA as well as induce mitochondrial damage that leads to cell apoptosis.[23] Rhodium complexes with trichlorido-5,6-dimethyl phenanthroline ligands display high cytotoxicity toward Jurkat leukemia cells and induce apoptosis by overproduction of ROS.[24] Furthermore, cellular metabolic studies of the rhodium complexes demonstrated that the apoptotic cell death is time dependent with moderate induction of ROS, which indicated the involvement of an activated intrinsic mitochondria-mediated pathway.[25] Moreover, rhodium complexes with phenylquinoline ligands are known as potent kinase C (PKCδ) inhibitors, and kinase C is regarded as a critical regulator for various cellular functions.[26] The racemic cyclometalated rhodium (III) complexes are promising inhibitors of JAK2 kinase activity, which acts as the critical cell signaling mechanism for cell proliferation and apoptosis. The abnormal activities of these kinases could be correlated with irregular cell growth and survival.[27]

The formation of transition metal complexes with biologically active ligands is an effective approach in the development of anticancer drugs. However, one major drawback of metal complexes is their instability in the cellular environment.[28] Therefore, the selection of an appropriate bidentate chelating ligand of oxygen and nitrogen, such as quinoline, bipyridine, phenanthroline, and their derivatives, has been proposed to improve the stability and cytotoxic activity of metal complexes.[29–31] Isoquinoline is a prerogative heterocyclic compound exhibiting anticancer, anti-Alzheimer, anti-inflammatory, anticonvulsant, and antimicrobial properties.[32] Recently, the tetrahydroisoquinoline derivative trabectedin was approved by the United States Food and Drug Administration (USFDA (2007)) and the European Commission (2015) for the treatment of soft tissue sarcoma.[33] Also, we previously reported that gold complexes with bioactive isoquinoline derivatives display high anticancer activity, selectivity, and synergistic effects against different cancer cell lines.[34] Inspired by the anticancer activity of metal complexes with isoquinolines, here, we synthesized palladium(II) and rhodium(III) complexes with isoquinoline derivatives and investigated their in vitro anticancer activity through the ROS/endoplasmic reticulum (ER)-stress-mediated and the autophagic cell death pathways. The in vivo anticancer activity of $[Pd(L^1)Cl_2]$ (**C1**) was also conducted on tumor xenograft model of mice bearing HepG2.

Experimental Methods

Materials

The chemicals were purchased from Alfa Aesar (Ward Hill, MA) and Sigma-Aldrich (St. Louis, MO) and used without further purification. Tris-buffered saline (TBS) solution (50 mM NaCl, 5 mM Tris) of pH 7.4 was prepared in double-distilled water. For the in vitro cytotoxicity assays, 2 mM stock solution of metal complexes was prepared in dimethyl sulfoxide (DMSO). Similarly, 2 mM solution of cisplatin was prepared in 0.9% NaCl saline. The working solutions were prepared from stock solution by serial dilution with TBS. Elemental analysis was used to determine the purity of each complex, which were ≥95%.

Instrumentation

A PerkinElmer 2400 Series II elemental analyzer was used for elemental analysis. Electrospray ionization mass spectrometry (ESI-MS) spectra were recorded on a Bruker HCT Spectrometer. A Bruker AV–600 nuclear magnetic resonance (NMR) spectrometer was used for the recording of ^{1}H and ^{13}C NMR spectra.

Synthesis and characterization

Ligands synthesis

1-(2′-Aminophenyl)-6,7-dimethoxy-isoquinoline (L^1), 1-(2′-aminophenyl)-6-methoxy-3,4-dihydroisoquinoline (L^2), and 1-(2′-aminophenyl)-6-methoxy-isoquinoline (L^3) were synthesized by the reported Bischler–Napieralski reaction.[35]

Spectroscopic data of L^1

Infrared (IR) (KBr, cm^{-1}): 3328 (N–H), 2927 (C–H), 2852 (Ar–H), 1623 (C=N), 1577, 1500 (C=C), 1247, 1115 (C–C), 872, 756, 653. ^{1}H NMR [500 MHz, $(CD_3)_2SO$, δ]: 8.43 (d, J = 4.6 Hz, 1H), 7.68 (d, J = 4.6 Hz, 1H), 7.44 (s, 1H), 7.22 (m, 2H), 7.18 (s, 1H), 6.91 (d, J = 6.3 Hz, 1H), 6.75 (td, J = 0.9, 6.0 Hz, 1H), 5.11 (s, 2H) 3.98 (s, 3H), 3.75 (s, 3H). ^{13}C NMR [100 MHz, $(CD_3)_2SO$, δ]: 157.1, 157.0, 152.9, 150.1, 146.9,

DOI: 10.31635/ccschem.020.202000363
Citation: *CCS Chem.* **2020**, 2, 1626–1641
Citation denotes calendar and volume year of first online publication.
Issue Assignment: Volume 3 (2021), Issue 6

141.1, 131.2, 129.5, 123.3, 122.7, 119.0, 116.4, 116.2, 105.9, 105.5, 56.2, 55.6 (Supporting Information Figures S1–S3).

Spectroscopic data of L^2

IR (KBr, cm^{-1}): 3409 (O–H), 3293 (N–H), 3184 (C–H), 2966, 2833 (Ar–H), 1606 (C=N), 1556, 1486, 1450 (C=C), 1252, 1107 (C–C), 833, 757, 682, 728. ^{1}H NMR [500 MHz, $(CD_3)_2$·SO, δ]: 2.72 (t, J = 7.2 Hz, 2H), 3.73 (t, J = 7.2 Hz, 2H), 3.83 (s, 3H), 5.83 (s, 2H), 6.58 (t, J = 7.1 Hz, 1H), 6.79 (d, J = 8.0 Hz, 1H), 6.85 (dd, J = 2.5, 8.6 Hz, 1H), 6.93 (d, J = 2.3 Hz, 1H), 7.04–7.14 (m, 3H). ^{13}C NMR [125 MHz, $(CD_3)_2$SO, δ]: 26.7, 47.2, 55.9, 112.3, 113.4, 115.4, 116.5, 121.1, 122.7, 129.8, 130.0, 131.0, 141.4, 148.4, 161.3, 166.4 (Supporting Information Figures S4–S6).

Spectroscopic data of L^3

IR (KBr, cm^{-1}): 3461 (O–H), 3329 (N–H), 3202, 3048 (C–H), 2922 (Ar–H), 1617 (C=N), 1553, 1456, 1410 (C=C), 1256, 1116 (C–C), 833, 682, 628. ^{1}H NMR [500 MHz, $(CD_3)_2$SO, δ]: 8.50 (d, J = 4.7 Hz, 1H), 7.77 (m, 3H), 7.44 (d, J = 2.1 Hz, 1H), 7.26 (dd, J = 2.1, 8.0 Hz, 1H), 7.22 (m. 1H) 7.12 (dd, J = 1.1, 6.2 Hz, 1H), 6.74 (m, 1H), 5.09 (s, 2H) 3.96 (s, 3H). ^{13}C NMR [100 MHz, $(CD_3)_2$SO, δ]: 160.6, 159.1, 146.9, 142.9, 139.2, 131.3, 129.6, 123.1, 122.6, 120.3, 119.5, 116.2, 116.1, 108.1, 105.4, 56.0 (Supporting Information Figures S7–S9).

General procedure for the formation of complexes

Metal salts (1 mmol) and ligands (0.5 mM) were dissolved in an equal volume of dichloromethane and methanol, and the total volume of 5 mL solvent was placed into a 25 cm-long glass Pyrex glass tube. The mixture was frozen by liquid nitrogen for 5 min, and the air was removed using a vacuum pump. The tube was sealed by fire torch. After 72 h of constant heating at 80 °C, block crystals were harvested. A suitable crystal was selected for single-crystal X-ray diffraction analysis. All the refinement description and crystal data are listed in Supporting Information Table S2.

$[Pd(L^1)Cl_2]$

After formation of the complex via the general procedure, block orange crystals of **C1** were harvested. A suitable crystal was selected for single-crystal X-ray diffraction analysis. Yield: 70%. Elemental analysis calcd for $C_{17}H_{16}Cl_2N_2O_2Pd$ (%): C, 44.62; H, 3.52; N, 6.12; found (%): C, 44.71; H, 3.35; N, 6.23. ^{1}H NMR (600 MHz, DMSO-d_6, δ): 8.66 (d, J = 12.0 Hz, 1H), 7.88–7.86 (m, 1H), 7.63–7.60 (m, 1H), 7.58 (s, 1H), 7.56 (d, J = 12.0 Hz, 1H), 7.47 (dd, J = 18.0, 12.0 Hz, 2H), 7.38 (s, 3H), 4.00 (s, 3H), 3.82 (s, 3H). ^{13}C NMR (150 MHz, DMSO-d_6, δ): 154.7, 153.1, 151.4, 144.0, 139.1, 135.4, 133.2, 132.5, 132.1, 125.1, 122.4, 121.5, 106.5, 106.1, 56.8, 56.1, 49.1. IR (KBr, cm–^{1}): 2971 (–OCH_3), 3128 (C–H), 1089 (C–N), 2381 (C=N), 3429 (N–H), 1614 (C=C), <400 (Pd–Cl), 412 (Pd–N). ESI-MS: m/z = 480.95 $[M + Na]^+$ (Supporting Information Figures S10–S13).

$[Rh(L^1)Cl_3(DMSO)]$

After formation of the complex via the general procedure, block yellow crystals of $Rh(L^1)Cl_3$(DMSO) (**C2**) were harvested. A suitable crystal was selected for single-crystal X-ray diffraction analysis. Yield: 65%. Elemental analysis calcd for $C_{19}H_{22}Cl_3N_2O_3RhS$ (%): C, 40.20; H, 3.91; N, 4.93; S, 5.65; found (%): C, 40.33; H, 4.01; N, 5.04; S, 5.76. ^{1}H NMR (600 MHz, DMSO-d_6, δ): 9.33 (d, J = 6.0 Hz, 1H), 8.39 (d, J = 12.0 Hz, 1H), 7.92 (d, J = 12.0 Hz, 1H), 7.73 (d, J = 6.0 Hz, 1H), 7.58 (s, 1H), 7.48 (s, 1H), 7.43 (dd, J = 12.0, 6.0 Hz, 1H), 7.34 (dd, J = 12.0, 6.0 Hz, 2H), 5.76–5.71 (m, 1H), 4.03 (s, 3H), 3.81 (s, 3H), 3.53 (s, 3H), 3.43 (s, 3H). ^{13}C NMR (150 MHz, DMSO-d_6, δ): 156.2, 154.6, 150.7, 145.8, 142.0, 135.6, 134.3, 131.8, 130.4, 125.5, 124.1, 123.1, 120.2, 107.4, 105.8, 56.7, 56.0. IR (KBr cm $^{-1}$): 2919 (–OCH_3), 3017 (C–H), 1099 (C–N), 2323 (C=N), 3461 (N–H), 1614 (C=C), 1425 (S=O), 626 (Rh–S), <400 (Rh–Cl), 433 (Rh–N). ESI-MS: m/z = 588.93 $[M + Na]^+$ (Supporting Information Figures S14–S17).

$[Pd(L^2)Cl_2]$

After formation of the complex via the general procedure, block orange crystals of $[Pd(L^2)Cl_2]$ (**C3**) were harvested. A suitable crystal was selected for single-crystal X-ray diffraction analysis. Yield: 70%. Elemental analysis calcd for $C_{16}H_{16}Cl_2N_2OPd$ (%): C, 44.42; H, 3.95; N, 6.09; found (%): C, 44.53; H, 3.79; N, 6.18. ^{1}H NMR (600 MHz, DMSO-d_6, δ): 7.68 (d, J = 12.0 Hz, 1H), 7.61–7.58 (m, 1H), 7.50 (d, J = 12.0 Hz, 1H), 7.35–7.34 (m, 2H), 7.16 (d, J = 6.0 Hz, 1H), 7.02 (s, 2H), 6.93–6.91 (m, 1H), 4.79 (d, J = 18.0 Hz, 1H), 3.87 (s, 3H), 3.46–3.42 (m, 1H), 2.82–2.79 (m, 2H). ^{13}C NMR (150 MHz, DMSO-d_6, δ): 166.9, 163.3, 141.9, 139.7, 133.5, 133.1, 132.8, 131.9, 124.9, 121.2, 121.0, 113.4, 113.1, 56.2, 52.3. IR (KBr, cm^{-1}): 2913 (–OCH_3), 3004 (C–H), 1024 (C–N), 2230 (C=N), 3425 (N–H), 1634 (C=C), <400 (Pd–Cl), 419 (Pd–N). ESI-MS: m/z = 426.9 [M–H]– (Supporting Information Figures S18–S21).

$[Rh(L^3)Cl_3(DMSO)]$

After formation of the complex via the general procedure, block yellow crystals of $Rh(L^3)Cl_3$(DMSO) (**C4**) were harvested. A suitable crystal was selected for single-crystal X-ray diffraction analysis. Yield: 60%. Elemental analysis calcd for $C_{18}H_{20}Cl_3N_2O_2RhS$ (%): C, 40.21; H, 3.75; N, 5.21; S, 5.96; found (%): C, 40.35; H, 3.71; N, 5.36; S, 5.35 ^{1}H NMR (600 MHz, DMSO-d_6, δ): 9.39 (d, J = 6.0 Hz, 1H), 8.44 (s, 1H), 8.09 (d, J = 6.0 Hz, 1H), 7.97 (d, J = 12.0 Hz, 1H), 7.57 (d, J = 6.0 Hz, 1H), 7.52 (d, J = 6.0 Hz, 1H), 7.44–7.41 (m, 2H), 7.34–7.31 (m, 2H), 5.73 (s, 1H), 4.01 (s, 3H), 3.53 (s, 3H), 3.43 (s, 3H), 3.35 (s, 3H). ^{13}C NMR

DOI: 10.31635/ccschem.020.202000363
Citation: *CCS Chem.* **2020**, 2, 1626–1641
Citation denotes calendar and volume year of first online publication.
Issue Assignment: Volume 3 (2021), Issue 6

(150 MHz, DMSO-d_6, δ): 162.4, 158.7, 146.9, 142.1, 140.6, 134.9, 131.6, 131.4, 130.5, 125.4, 124.0, 122.6, 121.5, 120.6, 105.3, 56.5, 42.1, 41.8. IR (KBr, cm^{-1}): 3013 (–OCH_3), 3108 (C–H), 1019 (C–N), 2350 (C=N), 3440 (N–H), 1617 (C=C), 1411 (S=O), 679 (Rh–S), <400 (Rh–Cl), 413 (Rh–N). ESI-MS: $m/z = 558.92$ $[M + Na]^+$ (Supporting Information Figures S22–S25).

Single-crystal X-ray crystallographic analysis

A Bruker Smart APAX II was used at room temperature to collect X-ray data of complexes **C1**–**C4**. The monochromatic Mo-Kα radiation graphite source with wavelength of (λ = 0.71073 Å) was used for analysis. The direct method for the solvation of crystal structure was applied by using SHELXS-97.[36] And for refining all nonhydrogen atoms, a method of full-matrix least-squares on F_2 was applied with the thermal parameters of anisotropy by using SHELXL-97.[37] The atoms of hydrogen were isotropically located at calculated positions.

Cellular uptake of complexes

The cells were placed in a cell culture plate (100 mm) at 37 °C in a 5% CO_2 atmosphere for 24 h. Approximately 10 μM each of **C1**–**C4** complexes was added and incubation continued for 24 h. After 24 h the cells were washed, collected, and digested with HNO_3. Dilution was carried out by adding double-distilled water to 5% HNO_3. Inductively coupled plasma mass spectrometry (ICP-MS) was used for the measurement of metal content in the diluted solution.[38] The experiment was repeated three times and represented as mean ± SD.

For the determination of metal content in the mitochondria, nucleus, and cytoplasm, the cells were placed in a 70 mm plate at 37 °C for 24 h in a 5% CO_2 and 95% humidified atmosphere. The cells were treated and incubated for 24 h with **C1**–**C4** at a concentration of 10 μM. After the incubation, cells were washed three times with phosphate-buffered saline (PBS), and the Solarbio kit was used to extract mitochondria and nuclei, per the procedure given by the manufacturer. All the samples were treated with concentrated HNO_3 and dilution was done by adding double-distilled water up to 5% HNO_3 concentration. By using ICP-MS, the content of metal in the nucleus and mitochondria was measured. All these experiments were repeated three times and represented as mean ± SD.

Determination of lipophilicity

The flask-shaking method was used for the determination of lipophilicity of **C1**–**C4**. **C1** is used as an example to demonstrate the procedure here. A mixture of an equal volume of saturated stock solution of **C1** in octanol (saturated with NaCl of 0.9% W/V) and NaCl (0.9% W/V) aqueous (saturated with octanol) was shaken for 24 h on the oscillator. Both phases of water and oil were collected and were gently separated and dried under vacuum after centrifugation at 5000*g* for 5 min. The substance obtained was dissolved in 300 μM HNO_3 (65%) and diluted by Milli-Q water containing 10 parts per billion indium, to 5 milliliters. The concentration of **C1** (concentration of **C1** in octanol (Co) and concentration of **C1** in water (Cw)) was determined by ICP-MS using In as internal standard. The log Po/w values were calculated from Co/Cw.

Cell culturing and treatment

Dulbecco's modified eagle medium (DMEM) with fetal bovine serum (10%) was used for culturing cells. The cells were held in a 5% CO_2 humidified environment at 37 °C. The stock solution of **C1** (2 mM) was prepared in DMSO, and serial dilutions were performed to obtain the required working solutions in PBS.

Assay of in vitro cytotoxicity

The MTT (3-(4,5-dimethylthiazol-2-yl)-2,5-diphenyltetrazolium bromide) assay was used for the evaluation of the in vitro cytotoxicity. The cells with the density of 4×10^3 were cultivated in a flat-bottomed 96-well plate. The cells were treated with different concentrations of the complexes, ligands, and cisplatin for 48 h. Cisplatin was dissolved in PBS and media containing <1% DMSO and used as the positive control. Negative control cells were supplemented with DMEM. MTT solution was added after the treatment with drugs and incubated for another 4 h. After adding DMSO to dissolve the formazan crystals and discarding the supernatant, the absorbance at 490/650 nm was measured on a microplate reader.[39] The cytotoxicity was assessed using the absorbance ratio of the treated cells and the control cells. Bliss method ($n = 5$) was used to measure the IC_{50} values, which show the sensitivity of cells toward complexes and ligands.

Cell cycle determination

Commercially available 70 mm plates were used for cell culturing. The cells were treated with **C1** for 24 h. The cells were collected after 24 h, then washed with PBS, and fixed in 70% ethanol for one night at –20 °C. After resuspension in RNAs and propidium iodide (PI), fluorescence-activated cell sorting (FACS) was used for analysis of the cells. Mod Fit LT (version 3.3; Variety Software House, Topsham, Maine, USA) software was used for cell cycle calculation.

Apoptosis assessment

The cells were cultivated for 24 h in a six-well plate. After treated with **C1**, the cells were collected, washed, and incubated with PI (5 μL) and annexin V (5 μL) for 25 min at 30 °C. The samples were protected from light during

DOI: 10.31635/ccschem.020.202000363
Citation: *CCS Chem.* **2020**, 2, 1626–1641
Citation denotes calendar and volume year of first online publication.
Issue Assignment: Volume 3 (2021), Issue 6

incubation with dyes. FACS was used for the analysis of cell apoptosis.

Mitochondrial membrane potential analysis

A lipophilic fluorescent (JC-1) dye was used for measurement of membrane potential of mitochondria. The cells were exposed to **C1** at different concentrations for 24 h. After the exposure with **C1**, the cells were washed, collected, and incubated for 25 min with JC-1 dye. Flow cytometry was used for the detection of membrane potential of mitochondria. The damage to the mitochondrial membrane was shown by the orange fluorescence accumulated in the mitochondria, whereas the dye monomeric form produced green fluorescence, which accumulated in the cytosol at the event of mitochondrial membrane damage.

Confocal microscopic studies of ROS generation in ER

HepG2 cells were seeded on the commercially available coverslip of poly-1-lysine with the density of 2×10^6 in six-well plates with complete medium. Six hours after treatment with **C1**, the cells were washed and incubated for 20 min with 25 mM of 2′,7-dichlorodihydrouorescein diacetate (H_2DCFDA) (488 nm/515 nm) at 37 °C. H_2DCFDA was replaced with prewarmed ER-Tracker Red (587 nm/615 nm) and the cells were incubated for 20 min. The cells were washed with ultrapure water, and the coverslips were placed on the slides and immediately analyzed with confocal microscopy by using suitable objective lenses and Zeiss FLUOWIEW viewer (Carl Zeiss (Oberkochen, Germany)).

Caspases determination

The cells were treated with **C1** for 24 h. Activated caspases were measured by using CaspGLOW kit after the treatment. The cells were then washed and incubated for 20 min with 0.5 mL of FITC-LEHD-FMK in the dark and immediately analyzed with FACS. The data were compared with the control.

Determination of intracellular Ca^{2+} levels

The cells were treated with **C1** and cisplatin for 24 h. The intracellular level of Ca^{2+} was determined by using Fluo-3Am (fluorescent dye). Afterwards, the cells were washed and incubated for 25 min with (5 μM) Fluo-3Am in the dark and immediately analyzed with FACS at 525 nm wavelength of excitation. The dye was broken down into Am (Acetoxymethyl) and Fluo-3 by intracellular esterase when crossing the cell membrane. The Fluo-3 bound with cellular Ca^{2+} resulting in a strong fluorescence on excitation wavelength of 488 nm.

Western blot analysis

The total protein was collected by incubating the cells in lysis buffer, and the BCA (the bicinchoninic acid assay) Protein Assay kit was used for the determination of protein concentration. Equal amount (25 μg) of protein was loaded in the lanes of sodium dodecyl sulfate-polyacrylamide gel electrophoresis (SDS-PAGE) gel (10%). The proteins were then transferred to poly (vinylidene difluoride) (PVDF) membrane for 1 h at 120 V after the electrophoresis were done. The membrane was placed in a solution containing the primary antibody at 4 °C for 8 h and incubated in nonfat milk dissolved in TBST (Tris-Buffered Saline, 0.1% Tween) for 2.5 h at pH 7.4. The membrane was then incubated for 2 h with a secondary antibody conjugated with horseradish peroxidase at room temperature. TBST was used for washing the membrane, and signals were obtained by using the enhanced chemiluminescent kit (Western Blotting Kit of Peirce ECL).

In vivo anticancer activity

Nude mice from Peking Union Medical College (Beijing, China) were used in this study. All the mice were housed at Guangxi Medical University facilitation center for experimental animals in a controlled environment of temperature, humidity, and 12 h light and dark cycle. Commercially available food was provided to the animals. The studies were performed per Guangxi Medical University's Guide for the Caring and Use of Laboratory Animals. Tumor-bearing mice were divided into four groups containing six mice in each group. The cisplatin was dissolved in 0.9% saline. Similarly, a saline solution of 0.9% was used for vehicle control. When the diameter of the tumor reached 1.4 cm (day 0), the cisplatin or **C1** was injected intraperitoneally. The cisplatin (2 mg/kg) and **C1** (5 and 10 mg/kg) were administrated every 2 days. The volume of tumor was calculated in mm^3 by using the given formula: volume of tumor = 0.5 × (longest diameter) × (shortest diameter)^2. The growth curves of tumors were drawn as the number of days after the first treatment against the average tumor volume. The mice were sacrificed after 14 days of treatment. The tumor was collected and weighed, and formalin was applied for fixing in paraffin embedding. The given formula was used to calculate the tumor growth inhibition rate (IRT): IRT = 100% – (mean tumor weight of the control group – mean tumor weight of the experimental group)/mean tumor weight of the control group.[40]

Statistics

SPSS (version 13.0, Armonk, New York, USA) was used for data processing, including the Student's *t* test. $p \leq 0.05$ was considered statistically significant.

DOI: 10.31635/ccschem.020.202000363
Citation: *CCS Chem.* **2020**, 2, 1626–1641
Citation denotes calendar and volume year of first online publication.
Issue Assignment: Volume 3 (2021), Issue 6

Results and discussion

Synthesis and characterization of ligands and complexes

Three ligands of isoquinoline derivatives L^1, L^2, and L^3 were synthesized using the reported procedure. Ligand L^1 and L^3 differ only in the number and position of the methoxy group. L^1 has two methoxy groups at position 6 and 7, whereas L^3 has only one methoxy group at position 6. L^2 is a dihydroisoquinoline, which has only one methoxy group at position 6.[41] The ligands were characterized by NMR spectroscopy and IR spectroscopy.

All the complexes, including **C1**, **C2**, **C3**, and **C4** were prepared by mixing the ligand and corresponding metal salt in a thick Pyrex glass tube containing equal volume of dichloromethane and methanol as the solvent. The tube was sealed by fire torch. After 72 h of constant heating at 80 °C, block crystals were harvested. The complexes were characterized by elemental analysis, NMR, IR, and ESI-MS (Scheme 1). In addition, the stability of complexes **C1**–**C4** was determined under physiological conditions of pH 7.4 in TBS and Tris–KCl–HCl buffer by UV–visible spectroscopy and high-performance liquid chromatography (HPLC). The results indicated that complexes **C1**–**C4** are stable under physiological conditions for 48 h (Supporting Information).

Crystal structure of complexes

The crystal structures of the four complexes were determined by single-crystal X-ray diffraction analysis (Figure 1). Selected bond angles and bond lengths are reported in Supporting Information Table S1. **C1** and **C3** showed distorted square planar geometry. In both complexes, two atoms of chlorine and the heterocyclic nitrogen of bidentate isoquinoline ligand L^1 and L^2 are coordinated with Pd(II). In **C1**, the bond lengths between palladium and nitrogen are Pd–N1 = 2.031 Å and Pd–N2 = 2.036 Å, whereas the bond lengths for palladium and

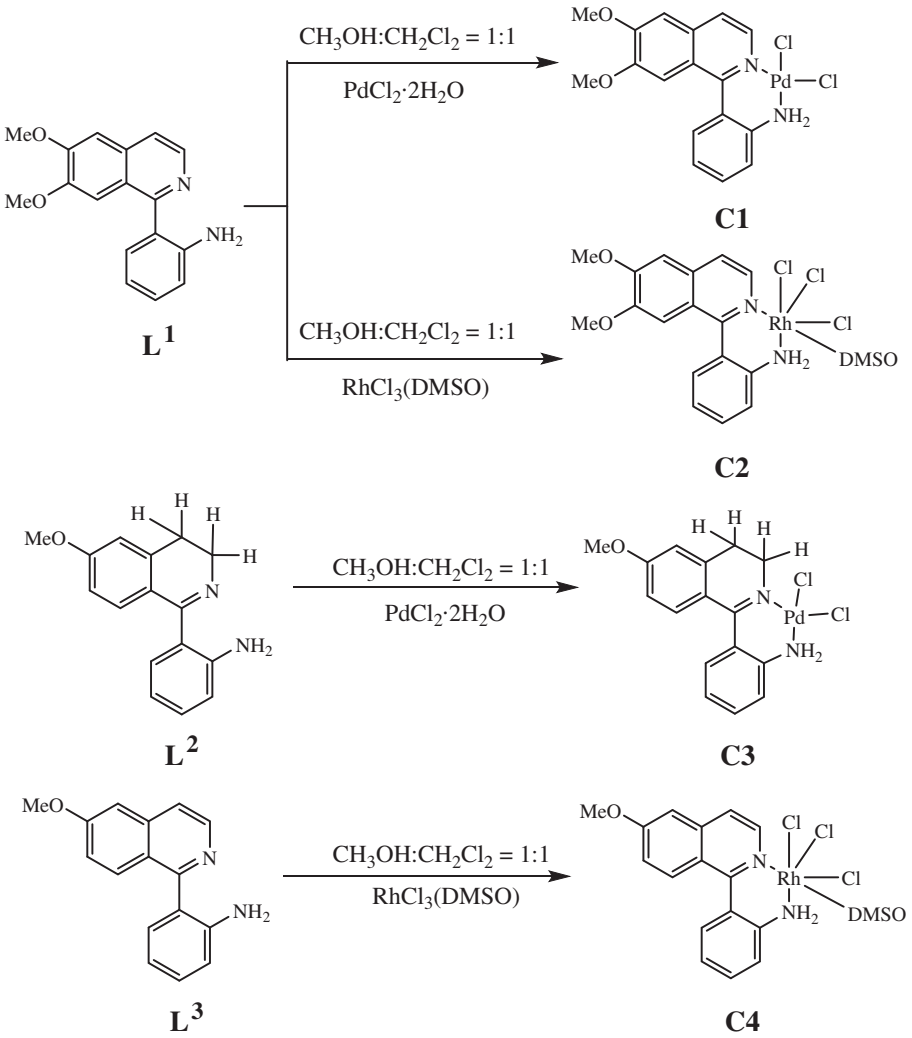

Scheme 1 | *Synthetic routes for complexes **C1**–**C4**.*

DOI: 10.31635/ccschem.020.202000363
Citation: *CCS Chem.* **2020**, 2, 1626–1641
Citation denotes calendar and volume year of first online publication.
Issue Assignment: Volume 3 (2021), Issue 6

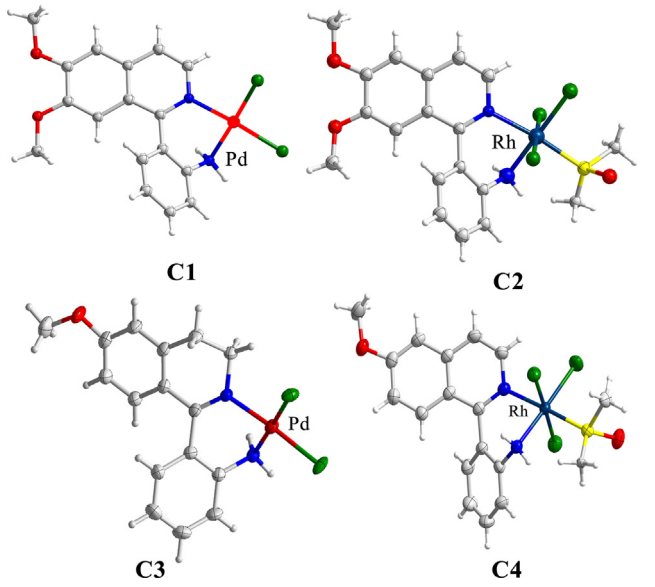

Figure 1 | *Crystal structures of **C1**–**C4**.*

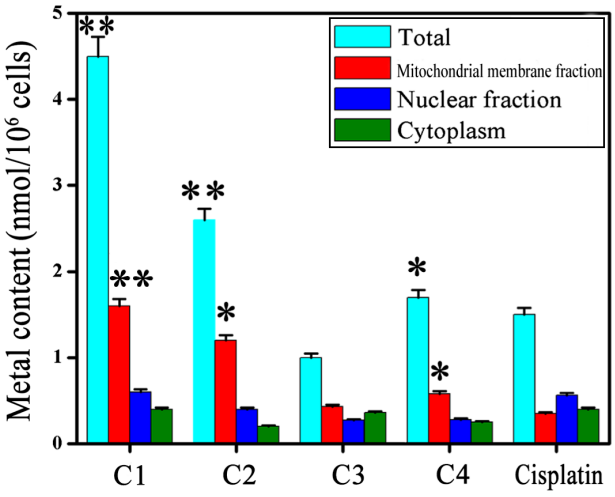

Figure 2 | *Analysis of metal content in whole cells, mitochondria, nucleus, and cytoplasm of HepG2 cells treated with **C1**–**C4** and cisplatin for 24 h performed by ICP-MS. Mean ± SD: *p < 0.05 and **p < 0.01.*

chlorine are Pd–Cl1 = 2.282 Å and Pd–Cl2 = 2.305 Å. In **C3**, the bond lengths between palladium and nitrogen are Pd–N1 = 2.035 Å and Pd–N2 = 2.033 Å, whereas the bond lengths for palladium and chlorine are Pd–Cl1 = 2.993 Å and Pd–Cl2 = 2.984 Å. The **C2** and **C4** complexes have six-coordinated distorted octahedral geometry in which one bidentate L^1 or L^3, three chlorine atoms, and one S from DMSO are coordinated with Rh(III). The Rh–N2 (Rh1–N2 and Rh2–N2) of the bidentate ligands (L^1 or L^3) and Rh–S1 (Rh1–S1 and Rh2–S1) are located perpendicular to each other, and the three chlorine atoms and Rh–N1 (Rh1–N1 and Rh2–N1) are positioned to the basal part of the square. The corresponding bond lengths are as follows: Rh1–N2 = 2.13 Å, Rh2–N2 = 2.09 Å, Rh1–S1 = 2.27 Å, and Rh2–S1 = 2.25 Å.

In vitro cytotoxicity

The cytotoxicity of **C1**–**C4** was investigated by MTT assay against seven cancer cell lines, including T-24, SKOV-3, HepG2, MDA-MB216, MGC-803, A549, HeLa, and normal human cell line WI-38, with cisplatin as a positive control. The IC_{50} values obtained from the cell viability assay are listed in Table 1. When treated with L^1–L^3, no significant effect was observed on cell viability in any cell line, whereas significant impact was found in the case of complexes **C1**–**C4** with IC_{50} values ranging from 1.05 to 22.04 μM. Complexes **C1**–**C4** had higher cytotoxicity in the cancer cells than the corresponding ligands and metal salts. Among the four complexes, **C1** exhibited the highest in vitro anticancer activity against the tested cell lines, which is higher than that of cisplatin. Notably, **C1**

Table 1 | *IC_{50} (μM) Values of L^1–L^3 and Complexes **C1**–**C4** Against Seven Cancer Cell Lines and One Normal Cell*

Compounds	WI-38	T-24	SKOV-3	HepG2	MDA-MB216	MGC-803	A549	HeLa
L^1	>100	>100	>100	>100	>100	>100	>100	>100
L^2	>100	>100	>100	>100	>100	>100	>100	>100
L^3	>100	>100	>100	>100	>100	>100	>100	>100
$PdCl_2{\cdot}2H_2O$	>50	>50	>50	>50	>50	>50	>50	>50
$RhCl_3$(DMSO)	>50	>50	>50	>50	>50	>50	>50	>50
C1	29.04 ± 0.3	5.08 ± 0.4	6.07 ± 0.5	1.05 ± 0.4	4.05 ± 0.3	2.34 ± 0.9	3.04 ± 0.3	5.04 ± 0.3
C2	38.02 ± 0.2	11.03 ± 0.7	14.03 ± 0.6	9.03 ± 0.1	8.02 ± 0.4	13.03 ± 0.4	17.08 ± 0.4	9.03 ± 0.5
C3	48.02 ± 0.7	25.04 ± 0.6	27.02 ± 0.6	22.04 ± 0.6	34.05 ± 0.6	29.04 ± 0.5	35.06 ± 0.5	28.08 ± 0.1
C4	41.03 ± 0.1	16.02 ± 0.5	19.06 ± 0.2	14.02 ± 0.5	17.04 ± 0.6	21.35 ± 0.4	25.07 ± 0.1	19.04 ± 0.2
Cisplatin[a]	21.05 ± 0.3	27.02 ± 0.3	24.03 ± 0.6	11.5 ± 0.6	13.03 ± 0.4	19.4 ± 0.09	20.02 ± 0.8	22.03 ± 0.2

[a] The stock solution of cisplatin was made by dissolving 24 mg of powder in pure water (10 mL). The solution was placed at 4 °C. The required concentration was prepared in 0.9% NaCl solution. The quality of stock and working solution was checked for quality control before the performance of experiments.

DOI: 10.31635/ccschem.020.202000363
Citation: *CCS Chem.* **2020**, 2, 1626–1641
Citation denotes calendar and volume year of first online publication.
Issue Assignment: Volume 3 (2021), Issue 6

showed low cytotoxicity toward human normal cell line WI-38. Compared with **C3** and **C4**, complexes **C1** and **C2** exhibited lower IC_{50} values, which implies that the number and position of the methoxy group on the isoquinoline scaffold affect the cytotoxicity of the complexes. This result is consistent with the fact that **C1** and **C2** have higher lipophilicity (log Po/w values) than **C3** and **C4** (Supporting Information).

Determination of cellular uptake

The cytotoxic activity of metallic anticancer drugs correlates with their cellular uptake.[42] Comparatively, the HepG2 cells were most sensitive to the complexes among the tested cancer cell lines. Therefore, ICP-MS was used to examine the cellular uptake of **C1**–**C4** complexes in the HepG2 cell line. The cells were treated with equal concentrations of complexes (10 μM) for 24 h, and the whole cell lysate was extracted. The determined uptake amounts of **C1**–**C4** were in the order of **C1** > **C2** > **C4** > **C3**, agreeing with their lipophilicity. Generally, the mitochondria and nucleus are typically considered the main targets of metal complexes. Therefore, the distribution of these complexes in these two subcellular organelles as well as in cytoplasm was investigated. The amounts of metal in the whole cells (10^6 cells) treated with **C1**–**C4** and cisplatin

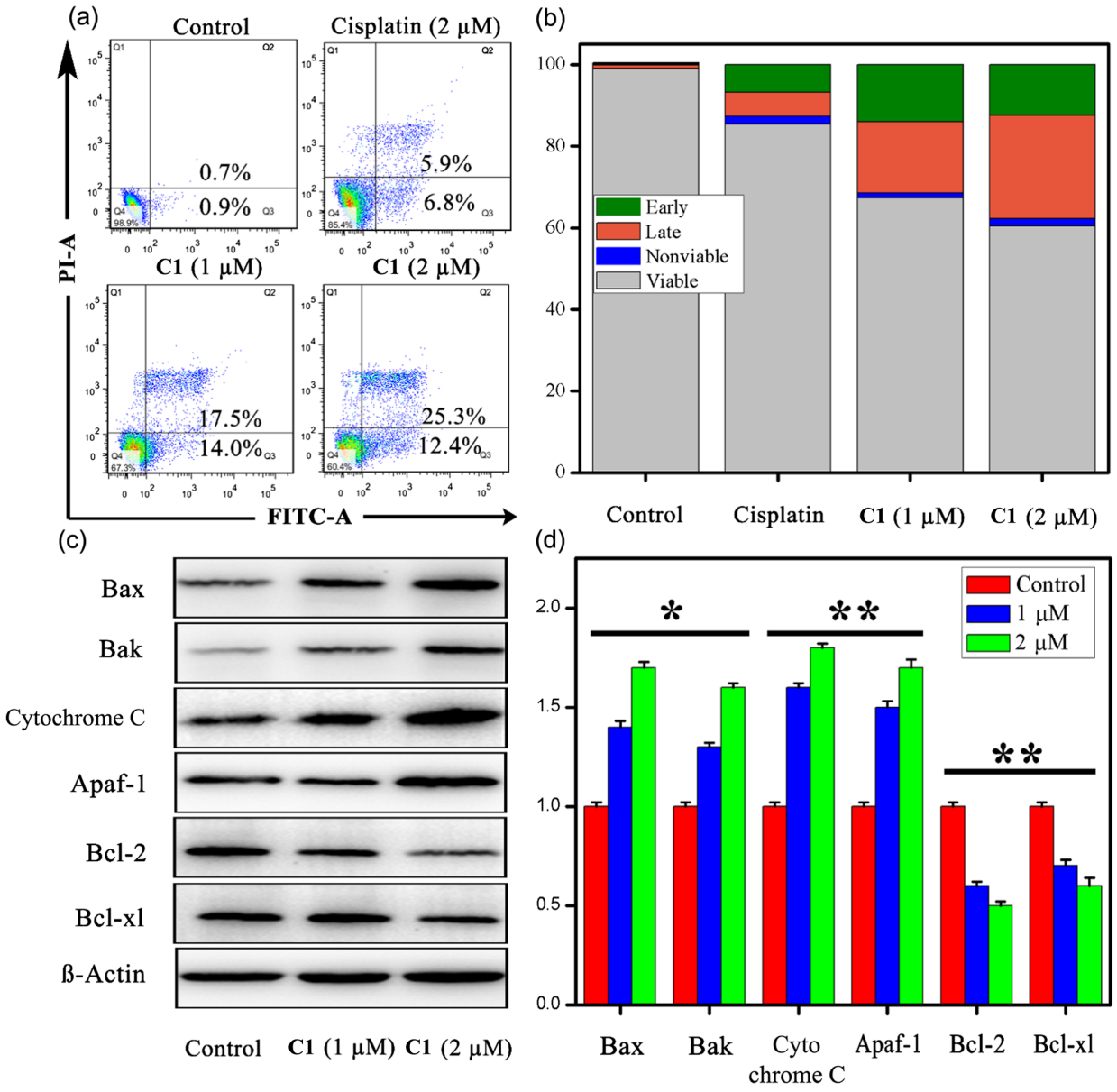

Figure 3 | *Analysis of apoptosis in HepG2 cells treated with **C1**. (a) Effect of **C1** and cisplatin on the apoptosis induction in HepG2 cells. (b) Histogram representing the percentage of cell population at late and early apoptosis. (c) The expression level of apoptosis-related proteins by Western blot. (d) Western blot quantification of bands by Image J. Mean ± SD: *p < 0.05 and **p < 0.01.*

DOI: 10.31635/ccschem.020.202000363
Citation: *CCS Chem.* **2020**, 2, 1626–1641
Citation denotes calendar and volume year of first online publication.
Issue Assignment: Volume 3 (2021), Issue 6

were 4.9, 2.6, 1.0, 1.7, and 1.5 nM, respectively. The amounts of **C1**–**C4** and cisplatin in mitochondria were determined to be 1.6, 1.25, 0.4, 0.6, and 0.3 nM, respectively. The concentration of **C1**–**C4** and cisplatin in the nucleus (10^6 cells) were determined to be 0.3, 0.2, 0.14, 0.16, and 0.3 nM, respectively. In addition, the concentration of these complexes in the cytoplasm were 0.2, 0.1, 0.18, 0.12, and 0.2 nM, respectively. These results indicated that the deposition of complexes in mitochondria was higher than that in the nucleus and cytoplasm, and the accumulation of **C1** in mitochondria was higher than the other three complexes. The optimal lipophilicity associated with these complexes contributed to the interaction with the lipophilic mitochondrial inner membrane, which facilitated the penetration into mitochondria. These findings also showed a significant correlation between the in vitro cytotoxicity and cellular uptake of **C1**–**C4** in HepG2 cells, and the mitochondria may be the target of **C1**–**C4** in HepG2 cells (Figure 2). Since the **C1** complex was the most effective against HepG2, we selected **C1** to investigate its anticancer mechanism and in vivo anticancer activity.

Apoptosis of HepG2 cells induced by C1

Mitochondrial dysfunction and ER-stress activate different pathways leading to cell death via apoptosis. For example, cisplatin induced acute apoptosis via the generation of high levels of ROS and ER-stress, not by DNA damage.[43,44] Therefore, we examined the apoptosis

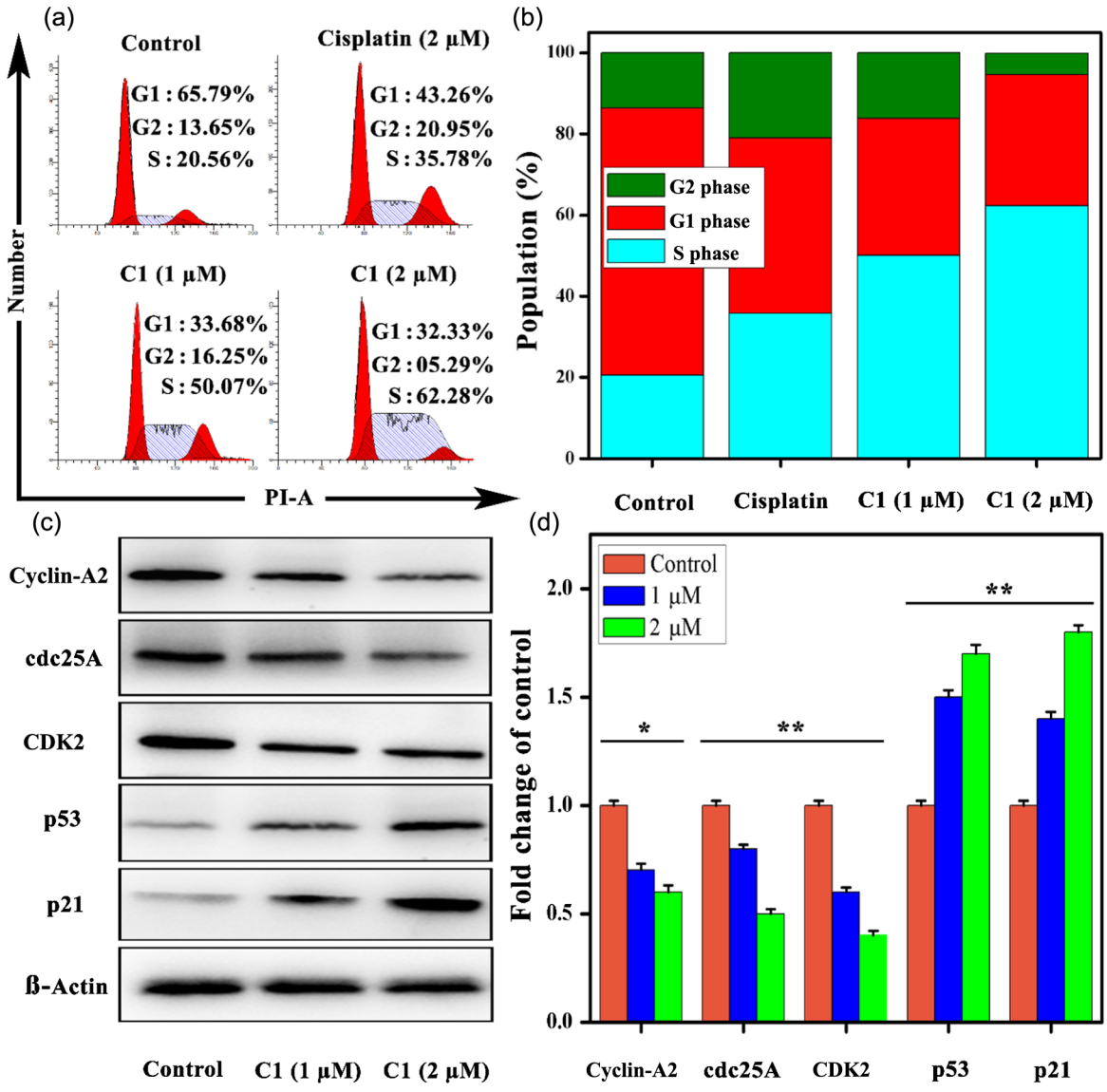

Figure 4 | *Analysis of cell cycle in HepG2 cells treated with **C1**. (a) Flow cytometric representation of cell cycle arrest of HepG2 cells. (b) A graphical representation of different phases of cell cycle. (c) The expression level of proteins related to cell cycle by Western blot. (d) Western blot quantification with Image J. Mean ± SD: *p < 0.05 and **p < 0.01.*

DOI: 10.31635/ccschem.020.202000363
Citation: *CCS Chem.* **2020**, 2, 1626–1641
Citation denotes calendar and volume year of first online publication.
Issue Assignment: Volume 3 (2021), Issue 6

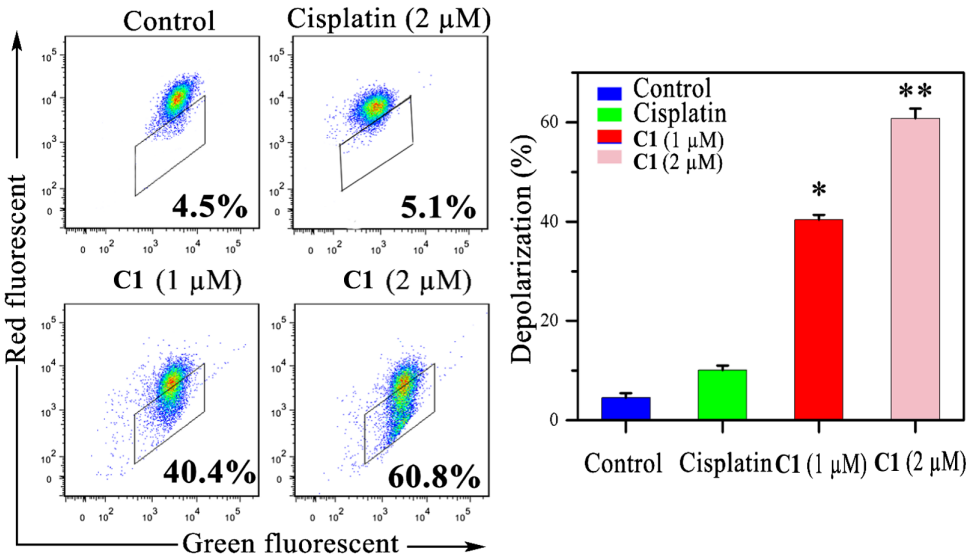

Figure 5 | *Analysis and graphical representation of mitochondrial membrane potential after exposure to **C1** and cisplatin. Mean ± SD: *p < 0.05 and **p < 0.01.*

induction ability of **C1** by using PI and annexin V staining. After the HepG2 cells were treated with different concentrations of **C1** (1 and 2 μM) for 24 h, a dose-dependent increase of late apoptotic cell population was observed. The late apoptotic cell population increased from 0.7% in the control to 17.5% and 25.3%, respectively (Figures 3a and 3b). Many chemotherapeutic agents induce apoptosis via mitochondrial-mediated pathways, which activate apoptotic cascades in cancer cells.[45] To examine the changes of apoptosis-related proteins after the treatment of HepG2 cells with different concentrations of **C1,** Western blotting analysis was carried out. The data indicated the upregulation of proapoptotic proteins (Bak, Bax, cytochrome C, and Apaf-1) and downregulation of antiapoptotic proteins (Bcl-2 and Bcl-xl) (Figures 3c and 3d).

Apoptosis follows different pathways; two pathways, the intrinsic and extrinsic (death receptor-dependent), are most important. These pathways are attributed to the activation of the caspase cascade, which results in the morphological and biochemical alteration of cells.[46] To explore the effect of **C1** on the activation of these pathways and the induction of mitochondrial-mediated apoptosis, the primary caspases including caspase-3 (executioner), caspase-8 (initiator), and caspase-9 were investigated. After the HepG2 cells were treated with **C1** (1 μM), the proteolytic activities of caspase-3 and caspase-9 (mitochondrial-mediated) increased from 0.01% and 3.78% in the control to 45.2% and 50.2%, respectively. Compared with these caspases, less change was observed for caspase-8, which is Fas/TNF mediated. This result showed that the apoptosis induced by **C1** occurred via the intrinsic mitochondrial pathway (Supporting Information Figure S35).

Cell cycle arrest

The cell cycle comprises a series of sequential events that control cell division and growth. To investigate whether **C1** inhibited the growth of tumor cells through cell cycle arrest, HepG2 cells were treated with different concentrations of **C1** and cisplatin and examined by flow cytometry using PI staining.[47] The flow cytometric data revealed that the percent population of cells in S-phase in the control was 20.56%, and it dose-dependently increased to 50.07% and 62.28% with the treatment of 1 and 2 μM **C1**, respectively. A comparatively less significant

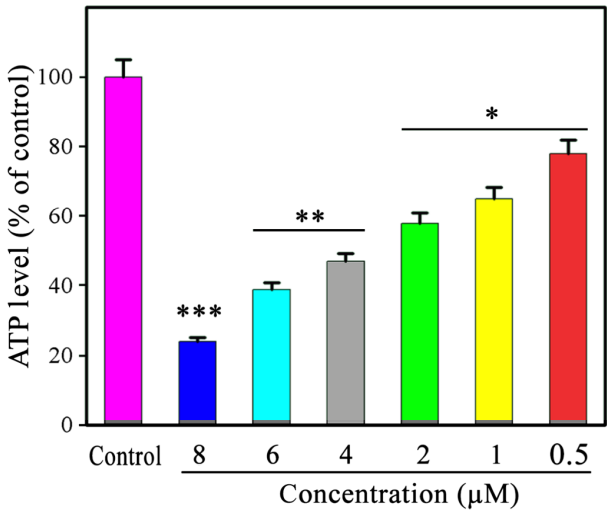

Figure 6 | *Cellular ATP level depletion with different concentrations of **C1**, recorded on microplate reader. *p < 0.05, **p < 0.01, and ***p < 0.001.*

DOI: 10.31635/ccschem.020.202000363
Citation: *CCS Chem.* **2020**, 2, 1626–1641
Citation denotes calendar and volume year of first online publication.
Issue Assignment: Volume 3 (2021), Issue 6

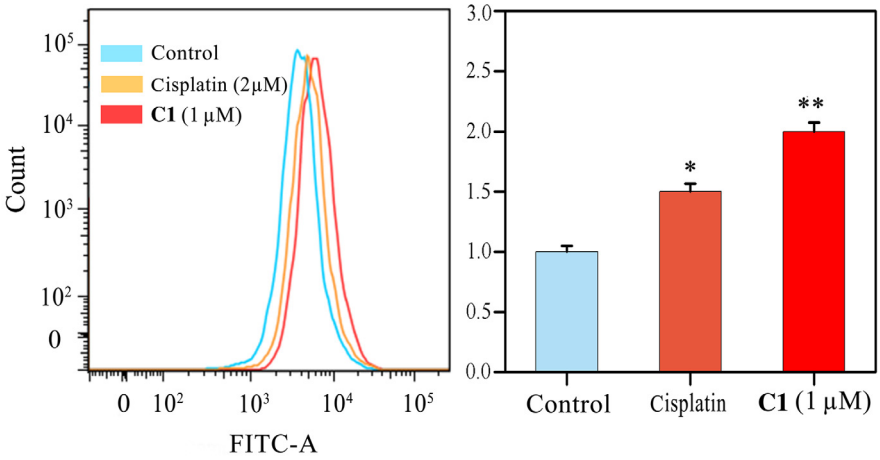

Figure 7 | *Flow cytometric analysis and graphical representation of ROS in HepG2 cells, after treatment with **C1** and cisplatin. Mean ± SD: *p < 0.05 and **p < 0.01.*

increase of cells in S-phase was observed after treatment with cisplatin (2 μM). The results demonstrated that cell cycle arrest at S-phase may be another mechanism of action of **C1** in HepG2 cells (Figures 4a and 4b). Cyclin-dependent kinase 2 (CDK2) plays a crucial role in the cell cycle G1–S phase transition, which is activated by cyclin-A and inhibited by p21.[48] The oncogenic protein (cdc25A) promotes the cell cycle from G1 to S phase. The inhibition of CDK2 by overexpressed p21, p53, and the degradation of cdc25A collectively arrest the cells in S phase.[49] Western blotting analysis indicated that the expressions of p53 and p21 proteins were upregulated, whereas the expressions of CDK2 and cdc25A were downregulated in HepG2 cells when treated with different concentrations of **C1**. These results provided strong evidence that **C1** regulated the cell cycle-related proteins, arrested cells in S phase, and induced apoptosis (Figures 4c and 4d).

Measurement of mitochondrial dysfunction

Mitochondria are recognized as a critical organelle integrating the death signals from intrinsic and extrinsic pathways. Therefore, mitochondrial damage and the release of death factors contribute to the initiation of apoptosis.[50,51] To investigate whether **C1** targeted mitochondria, the fluctuation of mitochondrial membrane potential, which is an indicator of mitochondrial dysfunction, was measured with a fluorescent dye probe JC-1. When the HepG2 cells were exposed to **C1**, the green fluorescence increased dose dependently as compared with the control. This result indicated that the mitochondrial membrane potential was affected by **C1**, suggesting mitochondrial membrane damage (Figure 5). The mitochondrial damage results in the alteration of various energy production pathways.[52] Therefore, a luminescence-based assay (Cell Titer-Glo) was used for the detection of changes in adenosine 5′-triphosphate (ATP) formation affected by **C1**. After HepG2 cells were treated with different concentrations of **C1**, a dose-dependent decrease in the intensity of ATP formation was observed. For instance, an 82.5 ± 0.5% decrease of ATP production was observed at the highest concentration of **C1** (8 μM). The results indicated that **C1** inhibited the ATP formation and impaired the mitochondrial energy metabolism of HepG2 cells. These results showed the involvement of mitochondrial damage in the apoptosis induced by **C1** (Figure 6).

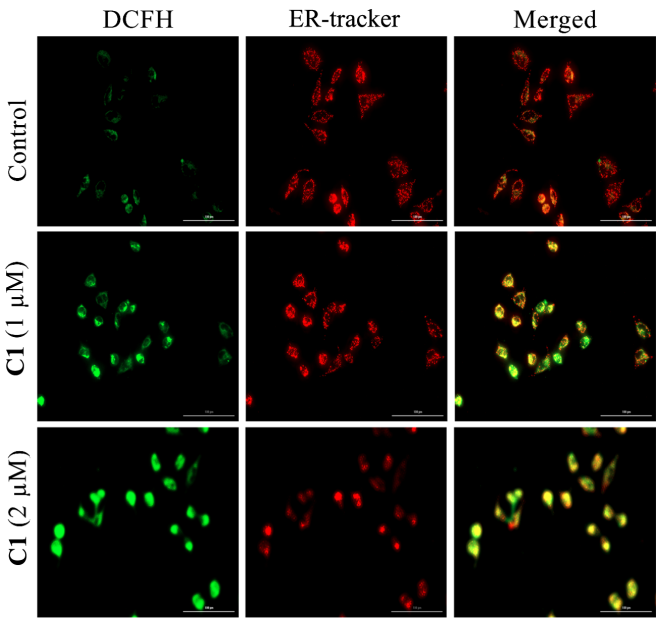

Figure 8 | *Confocal microscopic studies of HepG2 cells after treatment with **C1** [ROS generation indicated by green (DCFH) and ER-stress by ER-tracker red (Red)].*

DOI: 10.31635/ccschem.020.202000363
Citation: *CCS Chem.* **2020**, 2, 1626–1641
Citation denotes calendar and volume year of first online publication.
Issue Assignment: Volume 3 (2021), Issue 6

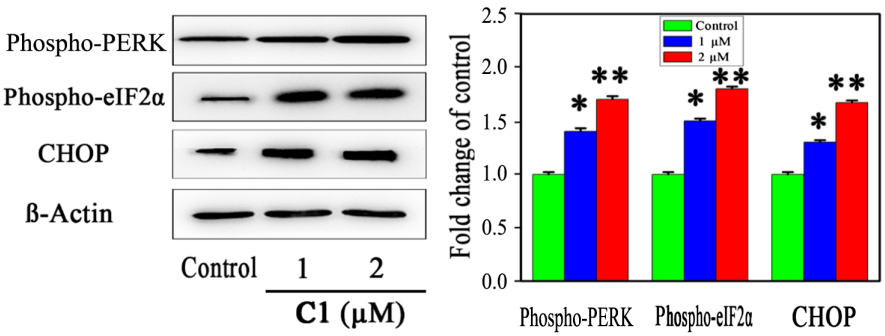

Figure 9 | *The expression and quantification of ER-stress related proteins in HepG2 cells after treatment with **C1**, using Image J for bands detection. Mean ± SD: *p < 0.05 and **p < 0.01.*

Generation of ROS and ER stress

Mitochondria are a major source of ROS, and therefore any damage to the mitochondria can cause an increase in the level of ROS, which leads to cellular dysfunction.[53] The ROS generation and induction of ER stress are regarded as the potential action mechanisms of anticancer drugs. Various cellular pathways are activated by the release of ROS.[54] Our results showed that **C1** induced cytotoxicity via the targeting of mitochondria, thus the effect of **C1** on the production of intracellular ROS was investigated by flow cytometry (Figure 7). In addition, confocal microscopy was also used for the detection of ROS generation and ER stress. The detection of ROS was carried out by using a dye, H_2DCFDA, which emits fluorescence upon oxidation to 2′,7′-dichlorofluorescein (DCF) by the cellular ROS. The ER was visualized by ER-Tracker Red, which binds to the ER sulphonylurea receptor. By means of confocal microscopy, the colocalization of ER and ROS was clearly observed at the concentration of 1 μM **C1**. When the concentration of **C1** was increased to 2 μM, the ROS signals were less colocalized and more defuse (Figure 8). These changes may result from the high permeability of the ER membrane, which could be correlated with the stress-induced death by the ER. Western blotting was carried out to further investigate the ER-stress-related proteins, such as C/EBP homologous proteins (CHOP), PKR-like ER kinase (PERK), and phosphorylated eukaryotic initiation factor 2α (eIF2α), after HepG2 cells were treated with 1–2 μM of **C1** for 24 h. The expression levels of CHOP, PERK, and eIF2α were upregulated, which could be associated with ER-stress-induced apoptosis (Figure 9).

Intracellular calcium production

The level of intracellular Ca^{2+} is important for the maintenance of mitochondrial membrane potential and the normal function of the ER. The ER is highly dependent on the Ca^{2+} concentration for the regulation of homeostasis. The imbalance of Ca^{2+} level contribute to the ER stress; accumulation of unfolded proteins such as CHOP, PERK, and eIF2α; and the depolarization of membrane potential of mitochondria, which in turn induce apoptosis.[55]

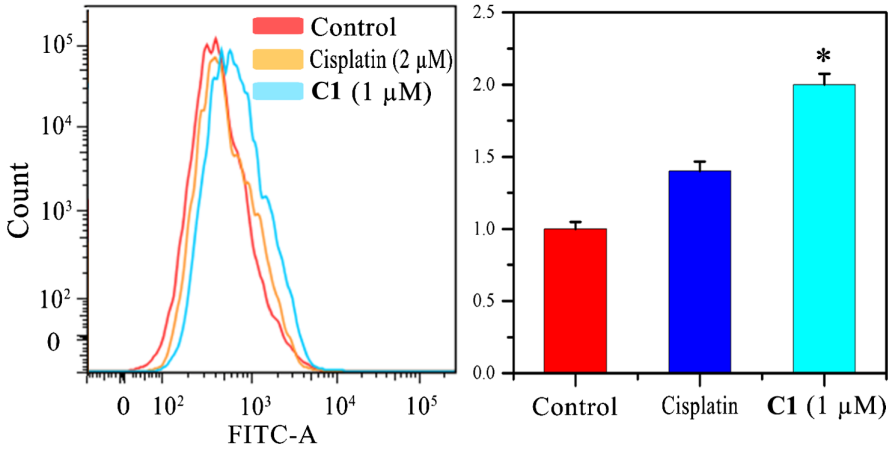

Figure 10 | *Flow cytometric determination of the intracellular calcium ions (Ca^{2+}) in HepG2 cells after treatment with **C1**. Mean ± SD: *p < 0.05.*

DOI: 10.31635/ccschem.020.202000363
Citation: *CCS Chem.* **2020**, 2, 1626–1641
Citation denotes calendar and volume year of first online publication.
Issue Assignment: Volume 3 (2021), Issue 6

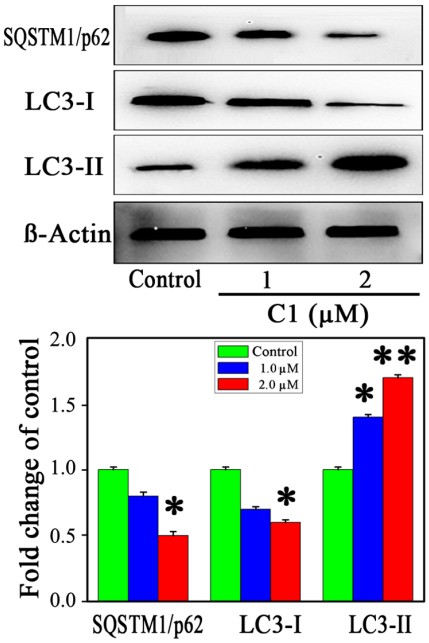

Figure 11 | *Expression levels of autophagy-related proteins in HepG2 cells after treatment with **C1**, quantified by Image J. Mean ± SD: *p < 0.05 and **p < 0.01.*

Therefore, we investigated the fluctuation of the Ca^{2+} level by using a fluorescent dye (Fluo-3 Am), whose fluorescence intensity increases by 60–70 times when bound with Ca^{2+}. HepG2 cells treated with **C1** (1 μM) exhibited a high level of Ca^{2+} as shown by the strong green fluorescence, compared with the negative control and cisplatin-treated cells. These findings demonstrated the imbalance in the Ca^{2+} level caused by **C1**, which could cause the mitochondria and ER-stress-mediated apoptosis (Figure 10).

Induction of autophagy

Morphologically cell death can be described in three modes: necrosis, apoptosis, and autophagy.[56] Autophagy is induced by stress signals, such as increased ROS, hypoxia, and mitochondrial damage.[57] To investigate whether **C1** induced cytotoxicity via autophagy, Western blotting was carried out to analyze some related proteins, such as LC3-I and LC3-II.[58] The results showed that the expression of LC3-II increased, whereas the expression of LC3-I decreased dose dependently. The increase of the LC3-II protein provided evidence of autophagy

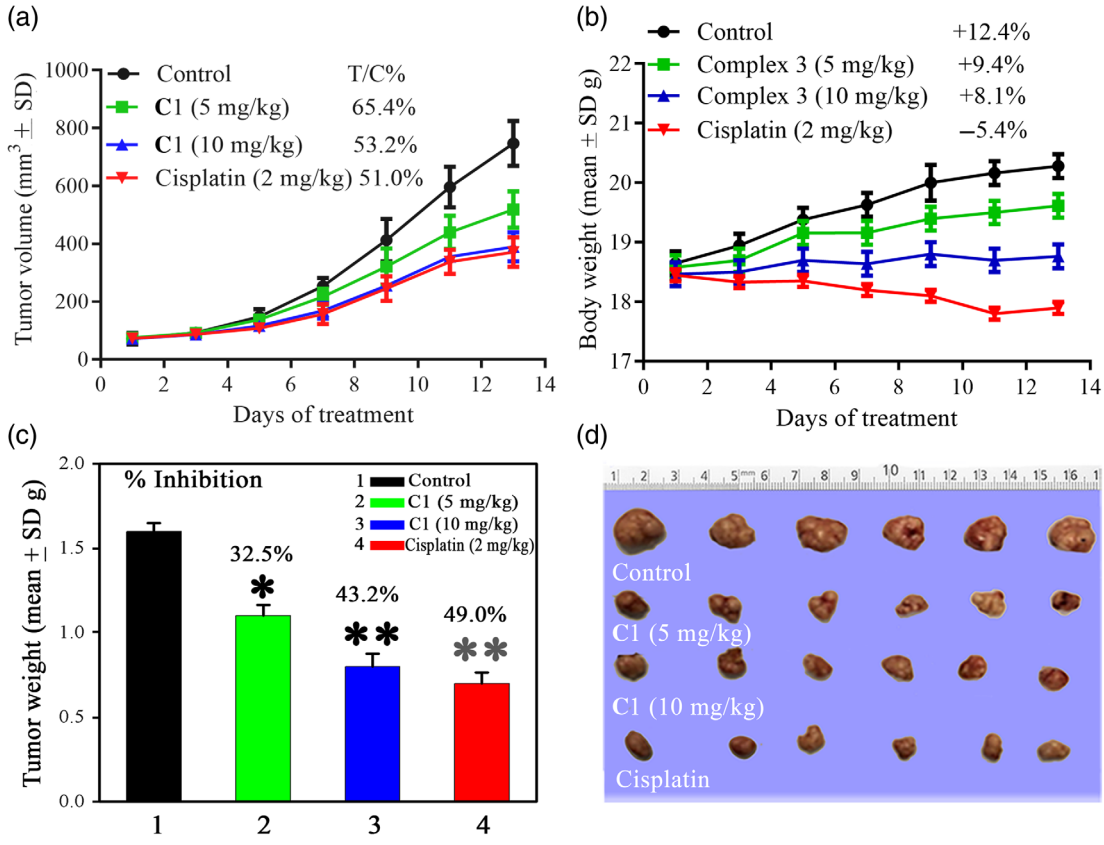

Figure 12 | *HepG2 tumor xenograft mice model. (a) Effect of **C1** and cisplatin on the growth of tumor volume. (b) Body weight of mice after treatment with **C1** and cisplatin. (c) Effect of **C1** and cisplatin on tumor weight expressed in percent inhibition values. (d). Photograph of tumors: negative control, **C1**-treated and cisplatin-treated group. Mean ± SD: *p < 0.05 and **p < 0.01.*

DOI: 10.31635/ccschem.020.202000363
Citation: *CCS Chem.* **2020**, 2, 1626–1641
Citation denotes calendar and volume year of first online publication.
Issue Assignment: Volume 3 (2021), Issue 6

induced by **C1**. The adaptor proteins p62 and sequestosome 1 (SQSTM1), help the conjugation of LC3 in misfolded proteins with ubiquitin moieties. Hence, the clearance of SQSTM1 and the ubiquitylated proteins mediated by the autophagic process further confirmed the induction of autophagy, as we found the downregulation of SQSTM1 in our experiment (Figure 11).[59]

In vivo anticancer activity of C1

A tumor xenograft mice model bearing HepG2 cells was used to investigate the in vivo anticancer activity of **C1**. The mice were divided into four groups, negative control, positive control, **C1** (lower dose), and **C1** (higher dose), with six mice in each group. The positive control group was treated with cisplatin (2 μM), and the negative control group was dosed with saline (V/V) containing 5% DMSO. The **C1**-treated groups were treated with low (5 mg/kg) and high doses (10 mg/kg) of **C1**. The treatments were continued for 14 days, and halted when the mice were sacrificed on day 14. The rates of tumor growth (IR) were measured for **C1**-low and **C1**-high dose, which were 32.5% and 43.2%, respectively. Tumor growth inhibition was observed in a dose-dependent manner (Figure 12a). The tumor inhibition rate of **C1** at high dose was comparable with that of cisplatin, which was 49.5% (Figure 12c). No apparent side effects and no substantial decrease in body weight were observed for **C1**, whereas a significant loss in bodyweight was observed for the group treated with cisplatin (Figure 12b).The apparent sizes of tumor were provided after the fourteen days treatment in Figure 12d. These findings suggested that **C1** showed similar tumor inhibition as cisplatin with fewer side effects.

Conclusion

Nonplatinum metal complexes **C1**–**C4** with isoquinoline derivatives as ligands were synthesized and fully characterized. The stability, cellular uptake, lipophilicity, and anticancer activity of complexes **C1**–**C4** were investigated. Among these complexes, **C1** demonstrated high antiproliferative activity toward selected cancer cell lines and low cytotoxicity against human normal cell line (WI-38) as compared with cisplatin. **C1** primarily targeted mitochondria resulting in the initiation of a sequence of events linked with mitochondrial dysfunction such as damage to the membrane potential, activation of the caspase cascade and release of cytochrome C, and the generation of a high amount of ROS and significant ER-stress response. Furthermore, **C1** not only activated the intrinsic mitochondrial pathway for apoptosis but also induced pro-death autophagy in HepG2 cells. A tumor xenograft mouse model showed that **C1** exhibited comparable anticancer activity but lower cytotoxicity with cisplatin. All these results suggested that **C1** is a potential anticancer drug candidate.

Supporting Information

Supporting Information is available.

Conflict of Interest

The authors declare no competing financial interest.

Funding Information

This work was supported by the National Natural Science Foundation of China (grant no. 21431001), IRT_16R15, and Natural Science Foundation of Guangxi Province of China (grant nos. 2016GXNSFGA380005 and AD17129007) as well as the "BAGUI Scholar" program of Guangxi Province of China.

Acknowledgments

The authors thank Ming Chen, Ke-Bin Huang, and Chun-Zhi Ai for their helpful discussions regarding the experimental design.

References

1. Thayer, A. M. Platinum Drugs Take Their Toll. *Chem. Eng. News* **2010**, *88*, 24–28.
2. Marques, M. P. M.; Gianolio, D.; Cibin, G.; Tomkinson, J.; Parker, S. F.; Valero, R.; Lopes, R. P.; de Carvalho, L. A. B. B. A Molecular View of Cisplatin's Mode of Action: Interplay with DNA Bases and Acquired Resistance. *Phys. Chem. Chem. Phys.* **2015**, *17*, 5155–5171.
3. Siddik, Z. H. Cisplatin: Mode of Cytotoxic Action and Molecular Basis of Resistance. *Oncogene* **2003**, *22*, 7265–7279.
4. Holford, J.; Sharp, S.; Murrer, B.; Abrams, M.; Kelland, L. In Vitro Circumvention of Cisplatin Resistance by the Novel Sterically Hindered Platinum Complex AMD473. *Br. J. Cancer* **1998**, *77*, 366–373.
5. Barton, J. K. Metals and DNA: Molecular Left-Handed Complements. *Science* **1986**, *233*, 727–734.
6. Banerjee, S. M.; El-Sheikh, S.; Malhotra, A.; Mosse, C. A.; Parker, S.; Williams, N. R.; MacRobert, A. J.; Hamoudi, R.; Bown, S. G.; Keshtgar, M. R. Photodynamic Therapy in Primary Breast Cancer. *J. Clin. Med.* **2020**, *9*, 483–294.
7. Cirri, D.; Fabbrini, M. G.; Pratesi, A.; Ciofi, L.; Massai, L.; Marzo, T.; Messori, L. The Leading Established Metal-Based Drugs: A Revisitation of Their Relevant Physico-Chemical Data. *Biometals* **2019**, *32*, 813–817.
8. Muhammad, N.; Guo, Z. Metal-Based Anticancer Chemotherapeutic Agents. *Curr. Opin. Chem. Biol.* **2014**, *19*, 144–153.

9. Wani, W. A.; Baig, U.; Shreaz, S.; Shiekh, R. A.; Iqbal, P. F.; Jameel, E.; Ahmad, A.; Mohd-Setapar, S. H.; Mushtaque, M.; Hun, L. T. Recent Advances in Iron Complexes as Potential Anticancer Agents. *New J. Chem.* **2016**, *40*, 1063–1090.
10. Cutillas, N.; Yellol, G. S.; de Haro, C.; Vicente, C.; Rodríguez, V.; Ruiz, J. Anticancer Cyclometalated Complexes of Platinum Group Metals and Gold. *Coord. Chem. Rev.* **2013**, *257*, 2784–2797.
11. Silva, T. M.; Fiuza, S. M.; Marques, M. P.; Persson, L.; Oredsson, S. Increased Breast Cancer Cell Toxicity by Palladination of the Polyamine Analogue N^1, N^{11}-Bis(ethyl)norspermine. *Amino Acids* **2014**, *46*, 339–352.
12. Vasdev, R. A.; Gaudin, L. F.; Preston, D.; Jogy, J. P.; Giles, G. I.; Crowley, J. D. Anticancer Activity and Cisplatin Binding Ability of Bis-Quinoline and Bis-Isoquinoline Derived $[Pd_2L_4]^{4+}$ Metallosupramolecular Cages. *Front. Chem.* **2018**, *6*, 1–9.
13. Rau, T.; Alsfasser, R.; Zahl, A.; van Eldik, R. Structural and Kinetic Studies on the Formation of Platinum(II) and Palladium(II) Complexes with L-Cysteine-Derived Ligands. *Inorg. Chem.* **1998**, *37*, 4223–4230.
14. Kljun, J.; Turel, I. β-Diketones as Scaffolds for Anticancer Drug Design—From Organic Building Blocks to Natural Products and Metallodrug Components. *Eur. J. Inorg. Chem.* **2017**, *2017*, 1655–1666.
15. Albert, J.; Bosque, R.; Crespo, M.; García, G.; Granell, J.; López, C.; Lovelle, M. V.; Qadir, R.; González, A.; Jayaraman, A. Cyclopalladated Primary Amines: A Preliminary Study of Antiproliferative Activity Through Apoptosis Induction. *Eur. J. Med. Chem.* **2014**, *84*, 530–536.
16. Ranninger, C. N.; Solera, I. L.; González, V. M.; Pérez, J. M.; Valdés, A. A.; Martín, A.; Raithby, P. R.; Masaguer, J. R.; Alonso, C. Cyclometalated Complexes of Platinum and Palladium with N-(4-Chlorophenyl)-α-Benzoyl-Benzylidene Amine. In Vitro Cytostatic Activity, DNA Modification, and Interstrand Cross-Link Studies. *Inorg. Chem.* **1996**, *35*, 5181–5187.
17. Hung, F. F.; Wu, S. X.; To, W. P.; Kwong, W. L.; Guan, X.; Lu, W.; Low, K. H.; Che, C. M. Palladium(II) Acetylide Complexes with Pincer-Type Ligands: Photophysical Properties, Intermolecular Interactions, and Photo-Cytotoxicity. *Chem. Asian J.* **2017**, *12*, 145–158.
18. Adiguzel, Z.; Baykal, A. T.; Kacar, O.; Yilmaz, V. T.; Ulukaya, E.; Acilan, C. Biochemical and Proteomic Analysis of a Potential Anticancer Agent: Palladium(II) Saccharinate Complex of Terpyridine Acting Through Double-Strand Break Formation. *J. Proteome Res.* **2014**, *13*, 5240–5249.
19. Ulukaya, E.; Ari, F.; Dimas, K.; Sarimahmut, M.; Guney, E.; Sakellaridis, N.; Yilmaz, V. T. Cell Death-Inducing Effect of Novel Palladium(II) and Platinum(II) Complexes on Non-Small Cell Lung Cancer Cells In Vitro. *J. Cancer Res. Clin. Oncol.* **2011**, *137*, 1425–1434.
20. Aliwaini, S.; Peres, J.; Kröger, W. L.; Blanckenberg, A.; Mare, J.; Edkins, A. L.; Mapolie, S.; Prince, S. The Palladacycle, AJ-5, Exhibits Anti-Tumour and Anti-Cancer Stem Cell Activity in Breast Cancer Cells. *Cancer Lett.* **2015**, *357*, 206–218.
21. Živanović, M. N.; Košarić, J. V.; Šmit, B.; Šeklić, D. S.; Pavlović, R. Z.; Marković, S. D. Novel Seleno-Hydantoin Palladium(II) Complex–Antimigratory, Cytotoxic and Pro-Oxidative Potential on Human Colon HCT-116 and Breast MDA-MB-231 Cancer Cells. *Gen. Physiol. Biophys.* **2017**, *36*, 187–196.
22. Cordier, C.; Pierre, V. C.; Barton, J. K. Insertion of a Bulky Rhodium Complex into a DNA Cytosine–Cytosine Mismatch: An NMR Solution Study. *J. Am. Chem. Soc.* **2007**, *129*, 12287–12295.
23. Bieda, R.; Kitanovic, I.; Alborzinia, H.; Meyer, A.; Ott, I.; Wölfl, S.; Sheldrick, W. S. Antileukemic Activity and Cellular Effects of Rhodium(III) Crown Thioether Complexes. *BioMetals* **2011**, *24*, 645–661.
24. Geldmacher, Y.; Rubbiani, R.; Wefelmeier, P.; Prokop, A.; Ott, I.; Sheldrick, W. S. Synthesis and DNA-Binding Properties of Apoptosis-Inducing Cytotoxic Half-Sandwich Rhodium(III) Complexes with Methyl-Substituted Polypyridyl Ligands. *J. Organomet. Chem.* **2011**, *696*, 1023–1031.
25. Geldmacher, Y.; Splith, K.; Kitanovic, I.; Alborzinia, H.; Can, S.; Rubbiani, R.; Nazif, M. A.; Wefelmeier, P.; Prokop, A.; Ott, I. Cellular Impact and Selectivity of Half-Sandwich Organorhodium(III) Anticancer Complexes and Their Organoiridium(III) and Trichloridorhodium(III) Counterparts. *J. Biol. Inorg. Chem.* **2012**, *17*, 631–646.
26. Dörr, M.; Meggers, E. Metal Complexes as Structural Templates for Targeting Proteins. *Curr. Opin. Chem. Biol.* **2014**, *19*, 76–81.
27. Leung, C. H.; Yang, H.; Ma, V. P. Y.; Chan, D. S. H.; Zhong, H. J.; Li, Y. W.; Fong, W. F.; Ma, D. L. Inhibition of Janus Kinase 2 by Cyclometalated Rhodium Complexes. *MedChemComm* **2012**, *3*, 696–698.
28. Hartinger, C. G.; Dyson, P. J. Bioorganometallic Chemistry—From Teaching Paradigms to Medicinal Applications. *Chem. Soc. Rev.* **2009**, *38*, 391–401.
29. Li, S.; Chen, Y.; Zhang, S.; More, S. S.; Huang, X.; Giacomini, K. M. Role of Organic Cation Transporter 1, OCT1 in the Pharmacokinetics and Toxicity of Cis-Diammine(pyridine) Chloroplatinum(II) and Oxaliplatin in Mice. *Pharm. Res.* **2011**, *28*, 610–625.
30. Štarha, P.; Trávníček, Z. Non-Platinum Complexes Containing Releasable Biologically Active Ligands. *Coord. Chem. Rev.* **2019**, *395*, 130–145.
31. Zunino, F.; Pratesi, G.; Formelli, F.; Pasini, A. Evaluation of a Platinum-Doxorubicin Complex in Experimental Tumor Systems. *Invest. New Drugs* **1990**, *8*, 341–345.
32. Jain, S.; Chandra, V.; Jain, P. K.; Pathak, K.; Pathak, D.; Vaidya, A. Comprehensive Review on Current Developments of Quinoline-Based Anticancer Agents. *Arab. J. Chem.* **2016**, *12*, 4920–4946.
33. Gordon, E. M.; Sankhala, K. K.; Chawla, N.; Chawla, S. P. Trabectedin for Soft Tissue Sarcoma: Current Status and Future Perspectives. *Adv. Ther.* **2016**, *33*, 1055–1071.
34. Khan, T. M.; Gul, N. S.; Lu, X.; Wei, J. H.; Liu, Y. C.; Sun, H.; Liang, H.; Orvig, C.; Chen, Z.-F. In Vitro and In Vivo Anti-Tumor Activity of Two Gold(III) Complexes with Isoquinoline Derivatives as Ligands. *Eur. J. Med. Chem.* **2019**, *163*, 333–343.
35. Sotomayor, N.; Domínguez, E.; Lete, E. Bischler–Napieralski Cyclization–*N*/*C*-Alkylation Sequences for the Construction of Isoquinoline Alkaloids. Synthesis of Protoberberines and Benzo[c]phenanthridines via

DOI: 10.31635/ccschem.020.202000363
Citation: *CCS Chem.* **2020**, 2, 1626–1641
Citation denotes calendar and volume year of first online publication.
Issue Assignment: Volume 3 (2021), Issue 6

C-2′-Functionalized 3-Arylisoquinolines. *J. Org. Chem.* **1996**, *61*, 4062–4072.
36. Sheldrick, G. M. Phase Annealing in SHELX-90: Direct Methods for Larger Structures. *Acta Crystallogr. A* **1990**, *46*, 467–473.
37. Sheldrick, G. M. SHELXL-97 Program for Crystal Structure Refinement. . In *SHELXS-97, Program for X-ray Crystal Structure Solution*; University of Göttingen: Göttingen Germany , **1997**.
38. Wei, J. H.; Chen, Z.-F.; Qin, J. L.; Liu, Y. C.; Li, Z. Q.; Khan, T. M.; Wang, M.; Jiang, Y. H.; Shen, W. Y.; Liang, H. Water-Soluble Oxoglaucine-Y(III), Dy(III) Complexes: In Vitro and In Vivo Anticancer Activities by Triggering DNA Damage, Leading to S Phase Arrest and Apoptosis. *Dalton Trans.* **2015**, *44*, 11408–11419.
39. Li, Y.; Tan, C. P.; Zhang, W.; He, L.; Ji, L. N.; Mao, Z. W. Phosphorescent Iridium(III)-bis-*N*-Heterocyclic Carbene Complexes as Mitochondria-Targeted Theragnostic and Photodynamic Anticancer Agents. *Biomaterials* **2015**, *39*, 95–104.
40. Zhang, G.; An, Y.; Lu, X.; Zhong, H.; Zhu, Y.; Wu, Y.; Yang, J.; Liu, Y.; Zhou, Z.; Peng, Y.; Chen, Z.-F. A Novel Naphthylamide Compound Restores p53 Function in Non-Small Cell Lung Cancer by Reorganizing the Bak and Bcl-xl Complex and Triggering Transcriptional Regulation. *J. Biol. Chem.* **2016**, *291*, 4211–4225.
41. Khan, T. M.; Gul, N. S.; Lu, X.; Kumar, R.; Choudhary, M. I.; Liang, H.; Chen, Z.-F. Rhodium(III) Complexes with Isoquinoline Derivatives as Potential Anticancer Agents: In Vitro and In Vivo Activity Studies. *Dalton Trans.* **2019**, *48*, 11469–11479.
42. Puckett, C. A.; Barton, J. K. Mechanism of Cellular Uptake of a Ruthenium Polypyridyl Complex. *Biochemistry* **2008**, *47*, 11711–11716.
43. Takuma, K.; Yan, S. S.; Stern, D. M.; Yamada, K. Mitochondrial Dysfunction, Endoplasmic Reticulum Stress, and Apoptosis in Alzheimer's Disease. *J. Pharmacol. Sci.* **2005**, *97*, 312–316.
44. Renvoize, C.; Biola, A.; Pallardy, M.; Breard, J. Apoptosis: Identification of Dying Cells. *Cell Biol. Toxicol.* **1998**, *14*, 111–120.
45. Xiong, S.; Mu, T.; Wang, G.; Jiang, X. Mitochondria-Mediated Apoptosis in Mammals. *Protein Cell* **2014**, *4*, 737–749.
46. Danial, N. N.; Korsmeyer, S. J. Cell Death: Critical Control Points. *Cell* **2004**, *116*, 205–219.
47. Malumbres, M.; Barbacid, M. Cell Cycle, CDKs and Cancer: A Changing Paradigm. *Nat. Rev. Cancer* **2009**, *9*, 153–166.
48. Graña, X.; Reddy, E. P. Cell Cycle Control in Mammalian Cells: Role of Cyclins, Cyclin-Dependent Kinases (CDKs), Growth Suppressor Genes and Cyclin-Dependent Kinase Inhibitors (CKIs). *Oncogene* **1995**, *11*, 211–220.
49. Sørensen, C. S.; Syljuåsen, R. G.; Falck, J.; Schroeder, T.; Rönnstrand, L.; Khanna, K. K.; Zhou, B. B.; Bartek, J.; Lukas, J. Chk1 Regulates the S Phase Checkpoint by Coupling the Physiological Turnover, and Ionizing Radiation-Induced Accelerated Proteolysis of Cdc25A. *Cancer Cell* **2003**, *3*, 247–258.
50. Bernardi, P.; Scorrano, L.; Colonna, R.; Petronilli, V.; Lisa, F. D. Mitochondria and Cell Death. *Eur. J. Biochem.* **1999**, *264*, 687–701.
51. Stock, D.; Leslie, A. G.; Walker, J. E. Molecular Architecture of the Rotary Motor in ATP Synthase. *Science* **1999**, *286*, 1700–1705.
52. Weinberg, S. E.; Chandel, N. S. Targeting Mitochondria Metabolism for Cancer Therapy. *Nat. Chem. Biol.* **2015**, *11*, 9–15.
53. Murphy, M. P. How Mitochondria Produce Reactive Oxygen Species. *Biochem. J.* **2009**, *417*, 1–13.
54. Simon, H. U.; Yehia, A. H.; Schaffer, F. L. Role of Reactive Oxygen Species (ROS) in Apoptosis Induction. *Apoptosis* **2000**, *5*, 415–418.
55. Rizzuto, R.; Giorgi, C.; Romagnoli, A.; Pinton, P. Ca^{2+} Signaling, Mitochondria and Cell Death. *Curr. Mol. Med.* **2008**, *8*, 119–130.
56. Hotchkiss, R. S.; Strasser, A.; McDunn, J. E.; Swanson, P. E. Cell Death. *N. Engl. J. Med.* **2009**, *361*, 1570–1583.
57. Ozben, T. Oxidative Stress and Apoptosis: Impact on Cancer Therapy. *J. Pharm. Sci.* **2007**, *96*, 2181–2196.
58. Klionsky, D. J.; Cuervo, A. M.; Seglen, P. O. Methods for Monitoring Autophagy from Yeast to Human. *Autophagy* **2007**, *3*, 181–206.
59. Moscat, J.; Meco, M. T. p62 at the Crossroads of Autophagy, Apoptosis, and Cancer. *Cell* **2009**, *137*, 1001–1004.

DOI: 10.31635/ccschem.020.202000363
Citation: *CCS Chem.* **2020**, 2, 1626–1641
Citation denotes calendar and volume year of first online publication.
Issue Assignment: Volume 3 (2021), Issue 6